Rotational 3D printing of damage-tolerant composites with programmable mechanics

Jordan R. Raney[a,b,1], Brett G. Compton[a,c,1], Jochen Mueller[d], Thomas J. Ober[a], Kristina Shea[d], and Jennifer A. Lewis[a,2]

[a]John A. Paulson School of Engineering and Applied Sciences and Wyss Institute for Biologically Inspired Engineering, Harvard University, Cambridge, MA 02138; [b]Department of Mechanical Engineering and Applied Mechanics, University of Pennsylvania, Philadelphia, PA 19104; [c]Department of Mechanical, Aerospace, and Biomedical Engineering, University of Tennessee, Knoxville, TN 37996; and [d]Engineering Design and Computing Laboratory, Department of Mechanical and Process Engineering, ETH Zurich, 8092 Zurich, Switzerland

Edited by Chad A. Mirkin, Northwestern University, Evanston, IL, and approved December 19, 2017 (received for review August 26, 2017)

Natural composites exhibit exceptional mechanical performance that often arises from complex fiber arrangements within continuous matrices. Inspired by these natural systems, we developed a rotational 3D printing method that enables spatially controlled orientation of short fibers in polymer matrices solely by varying the nozzle rotation speed relative to the printing speed. Using this method, we fabricated carbon fiber–epoxy composites composed of volume elements (voxels) with programmably defined fiber arrangements, including adjacent regions with orthogonally and helically oriented fibers that lead to nonuniform strain and failure as well as those with purely helical fiber orientations akin to natural composites that exhibit enhanced damage tolerance. Our approach broadens the design, microstructural complexity, and performance space for fiber-reinforced composites through site-specific optimization of their fiber orientation, strain, failure, and damage tolerance.

3D printing | composites | mechanics | bioinspired | damage tolerant

Natural composites generally possess exceptional mechanical properties, including high specific stiffness, strength, and damage tolerance due to their heterogeneity and structural complexity across multiple length scales (1). For example, wood exhibits high stiffness, high damage tolerance, and low density due to spatial variations in cellulose fiber alignment (2). Wood cell walls possess cellulose microfibrils that are arranged in layers and helically oriented with respect to the long axis of the cells. The helical angle of the cellulose microfibrils affects the elastic properties (3, 4) and the extensibility (5) of the wood, and varies spatially from the core wood to the outer mature wood as well as in response to environmental stresses that occur during growth (6, 7). Helical fiber arrangements have also been observed in other natural composites, such as the hammer-like stomatopod dactyl club (8), where extreme damage tolerance is required.

Engineered composites that combine oriented fibers and continuous matrices are widely used as structural materials. For example, polymer matrix composites (PMCs) and ceramic matrix composites incorporate woven fiber tows to mitigate brittle stochastic failure of individual fibers (9). In such composites, individual layers with different fiber orientations can be stacked to achieve quasi-isotropic elastic properties. Twisted bundles of ceramic fibers and helicoidal stacking of PMC laminae can also greatly enhance the fracture toughness and damage tolerance of engineered composites (10, 11). However, with the notable exception of 3D woven composites (12–14), the composite materials described above are predominantly processed as fabrics, reducing the effective utilization of fibers along particular orientations and making the formation of bulk components and complex geometries extremely costly. Efficient reproduction of the elegant and complex microstructures observed in nature remains elusive for engineered composites produced by conventional manufacturing methods (15).

Recent advances in additive manufacturing open new avenues for the design and fabrication of bioinspired, fiber-reinforced composites (16–21). For example, composites have been produced by fused filament fabrication of short fiber-filled thermoplastic filaments, which are melted and extruded through a hot printhead (16, 17, 19). Alternately, fiber-filled epoxy resins (18, 21), hydrogels (20), and elastomers have been printed under ambient conditions by direct ink writing (22–25), where the shear fields generated during ink extrusion through fine-deposition nozzles effectively aligns the fibers along the printing direction (20, 26, 27). Using this approach, lightweight cellular composites have been created in which the fibers are oriented horizontally within printed, high-aspect-ratio cell walls leading to enhanced specific stiffness (18). More recently, shape-morphing architectures have been created by printing hydrogel inks filled with cellulose fibrils into bilayers whose controlled variations in fiber alignment induce anisotropic swelling upon immersion in water (20). However, fiber alignment arises solely from the flow-induced shear field that these inks are subjected to within the deposition nozzle during printing and deterministically defined by the print path. Hence, within a given voxel ($\sim d^3$, where d = nozzle diameter and correspondingly the printed filament diameter), all fibers possess nearly the same orientation. By contrast, natural composites often rely on complex helical fiber arrangements that persist at small length scales (2, 8).

Recently, external fields have been coupled with 3D printing to impose greater control over fiber architecture and orientation in printed composites. For example, acoustic focusing within a direct-write deposition nozzle has been used to concentrate fibers within the center of printed filaments and strip off the excess carrier fluid (28, 29). Other groups have combined external magnetic fields with either direct ink writing or stereolithography to create polymer architectures in which fiber orientation is controlled voxel-by-voxel (30, 31). Although promising, fibers must interact strongly with the

Significance

Natural composites exhibit hierarchical and spatially varying structural features that give rise to high stiffness and strength as well as damage tolerance. Here, we report a rotational 3D printing method that enables exquisite control of fiber orientation within engineered composites. Our approach broadens their design, microstructural complexity, and performance space by enabling site-specific optimization of fiber arrangements within short carbon fiber–epoxy composites. Using this approach, we have created composites with programmable strain distribution and failure as well as enhanced damage tolerance.

Author contributions: J.R.R., B.G.C., T.J.O., and J.A.L. designed research; J.R.R., B.G.C., and J.M. performed research; J.R.R., B.G.C., J.M., and K.S. analyzed data; and J.R.R., B.G.C., J.M., K.S., and J.A.L. wrote the paper.

Conflict of interest statement: The authors have filed a patent on this work. J.A. Lewis has cofounded a company, Voxel8, which is focused on multimaterial 3D printing.

This article is a PNAS Direct Submission.

[1]J.R.R. and B.G.C. contributed equally to this work.

[2]To whom correspondence should be addressed. Email: jalewis@seas.harvard.edu.

This article contains supporting information online at www.pnas.org/lookup/suppl/doi:10.1073/pnas.1715157115/-/DCSupplemental.

applied field to quickly facilitate their reorientation within the carrier fluid. This requirement often limits the fiber concentration, geometry, and, hence, contribution to enhancing mechanical properties. Moreover, these approaches generate composites that possess a nearly uniform fiber alignment within any specific volume element.

Here, we report an additive manufacturing method that decouples fiber orientation from the prescribed print path used to construct the composites through the use of a rotational printhead that superimposes an additional shear field as ink is deposited through a cylindrical nozzle. Specifically, fibers can be locally reoriented as the ink exits the nozzle without requiring any coupling to external acoustic, magnetic, or electrical fields. Our approach, referred to as rotational direct ink writing (RDIW), can be applied to the broad array of materials that have been developed for extrusion-based 3D printing (18, 20, 23–25, 32). In RDIW, the rotation rate is defined independently from the print path, such that each voxel of printed material can itself be a spatially varying architecture of fibers giving rise to a mechanical response that varies locally from highly anisotropic to isotropic. Hence, RDIW enables the design and fabrication of engineered composites with site-specific optimization of fiber alignment, programmed strain distribution and failure, as well as enhanced damage tolerance.

Carbon fiber–epoxy composites have been widely used due to their combination of low density and high stiffness. To enable composite fabrication via rotational 3D printing, we developed viscoelastic inks composed of short carbon fiber-filled epoxy resins with varying fiber loading and resin composition. Each ink is designed to be shear thinning to facilitate flow through the rotating nozzle during printing and, as well, to possess a shear elastic modulus to retain their filamentary shape upon printing (Fig. S1). Specifically, three carbon fiber–epoxy inks are created (*Methods*); one with low fiber loading (1.3 vol % carbon fibers) to facilitate visualization and measurement of fiber orientation similar to previous work (18), another based on a flexible epoxy resin and higher fiber loading (15.5 vol % carbon fibers), and a final ink based on a brittle epoxy resin with an even higher fiber loading (18.5 vol % carbon fibers) that exhibits a much higher stiffness and a lower failure strain upon curing.

To achieve control over fiber alignment, a rotational printhead system is created in which a stepper motor controls the angular velocity (ω) of the rotating nozzle during direct writing of a viscoelastic fiber-filled epoxy ink (Fig. 1*A* and Movie S1). The rotational printhead is mounted on a 3D motion-controlled stage that controls translational velocity (v) and gap height (h) during direct ink writing (Fig. 1*B*). The nozzle radius (R) roughly defines a characteristic radius of the extruded filament. Different ratios of rotation rate and translational speed (ω/v) lead to different shear fields, which define a helical angle (φ) about the filament axis and align high-aspect-ratio fibers along these shear helices. We can control φ by actively modulating ω to impart the desired fiber orientation, from parallel to the printing direction ($R\omega/v = 0$), that is, φ = 0° (Fig. 1*C*), to helical (φ = 45° when $R\omega/v = 1$, as in Fig. 1*D*), to nearly perpendicular to the print path, that is, φ approaches 90° at sufficiently high rotation rates ($R\omega/v \sim 2$ or greater). Optical images and schematic cross-sectional views show the printed filaments in the absence (Fig. 1 *C* and *E*) and presence of rotation (Fig. 1 *D* and *F*). To quantify the effects of rotation rate on fiber alignment, we used the carbon fiber–epoxy resin ink with a dilute fiber loading (1.3 vol %), such that fiber orientation could be readily discerned using transmitted light (Fig. 1 *C* and *D*). We measured the fiber angle at the top surface of the printed filaments to determine the relationships between v, ω, and φ, as shown in Fig. 1*G*. The solid curve corresponds to the expected fiber orientation given by $\varphi = \tan^{-1}(R\omega/v)$ that arises from the idealized shear field imposed by the combined contributions of rotational rate and translational speed during printing. At intermediate values of the dimensionless rotation rate, that is, $0 < R\omega/v < 2.5$ for this ink, one can systematically tune the helical angle between nominally 0° and 60° over a broad range of printing speeds from 4 to 32 mm/s, with

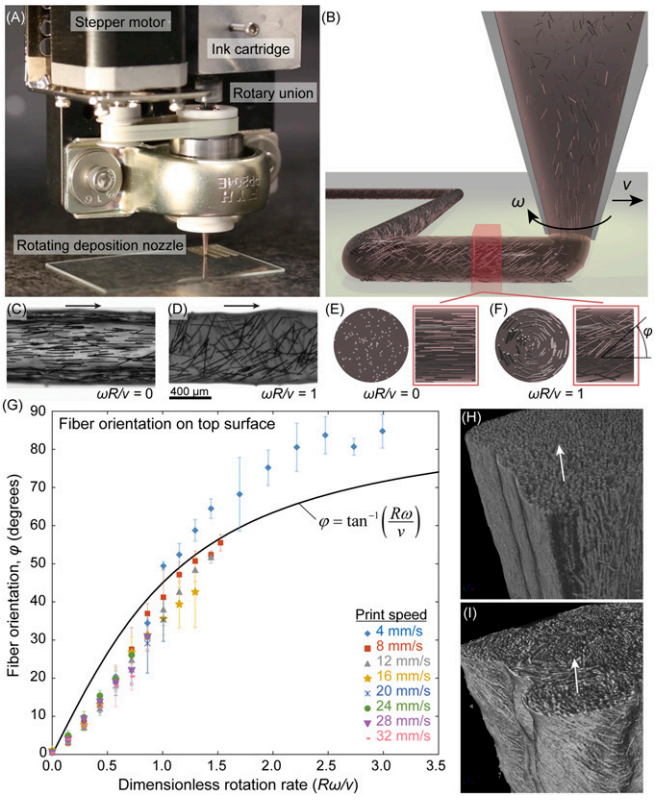

Fig. 1. Rotational 3D printing. (*A*) A stepper motor is directly interfaced with a 3D motion-control system to controllably rotate the deposition nozzle during printing. (*B*) Schematic view of fiber orientation during printing through the rotating nozzle to achieve a helical pattern, where the helical angle is dictated by the rotational rate (ω) and translational velocity (v). (*C* and *D*) Optical micrographs of fiber-filled epoxy filaments (1.3 vol % carbon fibers) printed without rotation and with a high rotation rate, respectively. (*E* and *F*) Idealized fiber arrangement shown schematically for the same dimensionless rotation rates. (*G*) Surface fiber orientation (φ) plotted as a function of dimensionless rotation rate ($R\omega/v$) over a wide range of rotational and translational rates, where the solid line denotes the kinematically ideal fiber orientation. (*H* and *I*) Cross-sectional views of the internal structure of composites printed without rotation and with a high rotation rate, respectively, as determined by X-ray microtomography (print direction indicated by arrow).

even higher helical angles obtained at the lowest printing speed. We also printed composites using concentrated epoxy inks with higher volume fractions (15.5–18.5 vol %) of carbon fibers, which confer superior mechanical properties. Since optical imaging is less effective at such high fiber loadings, we used X-ray microcomputed tomography (μCT) to observe the fiber alignment within the printed filaments (Fig. 1 *H* and *I*). Based on this simple kinematic model, the rotational shear should have its largest effect at the outer radius of the filament, where r is a maximum ($r = R$) defining a maximum helical angle of $\varphi = \tan^{-1}(R\omega/v)$ (Fig. 1 *E* and *G*) and the shear field should have no effect at the core of the filament, where $r = 0$ and, thus, φ = 0. Indeed, we observe a radial distribution of fiber orientation in the μCT images shown in Fig. 1 *H* and *I*.

To understand how variations in fiber alignment affect elastic mechanical properties, we printed tensile bars and measured their stiffness under quasistatic loading (Fig. 2). Using our flexible epoxy ink (15.5 vol % carbon fibers), we printed tensile bars with both longitudinal and transverse print paths that are aligned along and perpendicular to the direction of mechanical loading, respectively. Without rotation (far left of plot in Fig. 2*A*), these two print paths produce fiber alignments that are orthogonal to one another, resulting in highly anisotropic mechanical properties with a

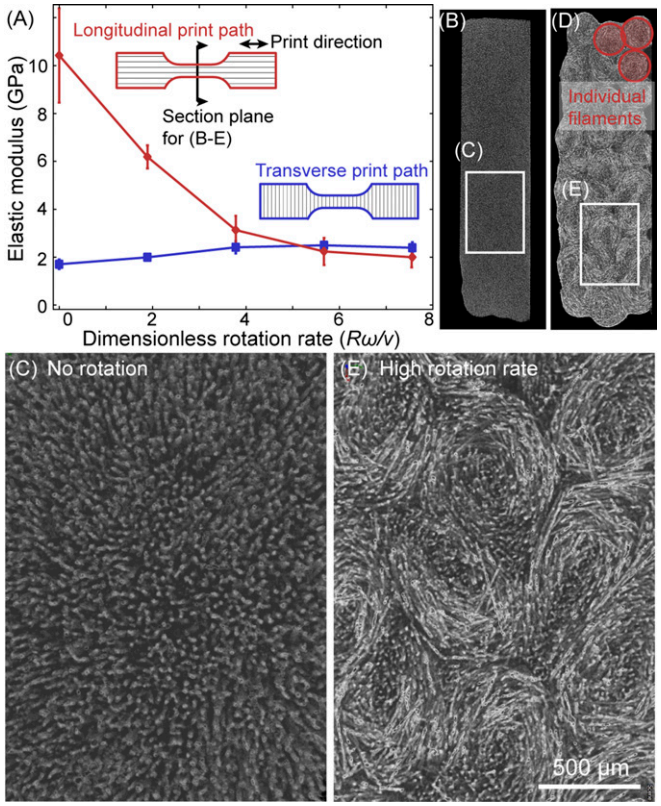

Fig. 2. Fiber orientation effects on elastic properties. (*A*) Plot of the measured elastic moduli as a function of dimensionless rotation rate for printed tensile bars composed of carbon-fiber-filled epoxy produced using either longitudinal (parallel with applied force) or transverse (perpendicular with applied force) print paths and varying rotation rates. (*B–E*) Images obtained by X-ray microtomography, which reveals the internal fiber orientation within these composite tensile bars printed with a longitudinal print path. (*B* and *D*) When no rotation is applied, the fiber orientation is highly uniform and nearly parallel along the print path. This anisotropic fiber arrangement leads to anisotropic elastic properties (i.e., the longitudinal elastic modulus is roughly 5× larger than the transverse elastic modulus). (*C* and *E*) By contrast, composite tensile bars printed at high rotation rates exhibit a more random fiber orientation and nearly isotropic elastic properties.

fivefold difference between the elastic modulus of the longitudinal ($E_L \sim 10$ GPa) and transverse ($E_T \sim 2$ GPa) tensile bars. Applying rotation produces helical fiber arrangements, as described in Fig. 1. As the rotation rate ω increases for a given translation speed v, the fiber orientation deviates by an increasing amount from the direction parallel to the print path, with an observed concomitant decrease in $E_L/E_T \sim 5$ when $R\omega/v = 0$ to $E_L/E_T \sim 1$ when $R\omega/v = 5$. This effect is observed directly by μCT, as shown for the longitudinal samples in Fig. 2 *B–E*. Without rotation, the fibers are nearly parallel to the longitudinal print path (Fig. 2 *B* and *C*), whereas they adopt a helical fiber arrangement within the printed filament when subjected to high rates of rotation (Fig. 2 *D* and *E*). If sufficiently high rotation rates ($R\omega/v \geq 5$) are used, there is a cross-over in the elastic moduli for samples printed with longitudinal and transverse print paths, respectively (Fig. 2*A*). In the cross-over region, even though their structure is not truly isotropic, their macroscopic elastic properties become effectively isotropic. Hence, one can create high-performance fiber-reinforced composites that are elastically isotropic simply by choosing an appropriate rotation rate for a given printing speed. Importantly, rotational 3D printing also allows engineered composites to be produced with programmable regions of highly anisotropic and isotropic mechanical properties simply by varying fiber orientation in a voxelwise manner, for example, near regions of stress concentration, to optimize their microstructure for a given loading condition.

To further demonstrate programmable control over mechanical properties, we printed carbon fiber–epoxy composites with sharply varying fiber alignment as a function of location using the same ductile epoxy ink formulation described above (Fig. 3). With appropriate modulation of rotational rate, fiber alignment can be changed from parallel to nearly perpendicular to the print path direction over distances on the order of the nozzle diameter, 2R (Movie S1). As shown in Fig. 3*A*, this composite is printed using a print path that is vertically oriented with respect to the image. Wherever the nozzle is not rotated, fibers are oriented along that same direction. At programmed locations, rotation is imposed to locally alter the fiber orientation within the matrix, yielding a rotated region in the form of an "H" (see Fig. S2 for additional examples). Using the experimentally determined elastic moduli, we carried out finite-element simulations to predict the strain field that would emerge in the presence of a force applied along the print path (revealing the H pattern in Fig. 3*B*; see Fig. S3 for details on finite-element analysis domain and mesh and Figs. S4–S7 for additional stress and strain fields). Due to the heterogeneity of the fiber orientations within the printed composite architecture, the applied strain does not distribute uniformly. The printed and cured samples, shown schematically in Fig. 3*A*, are coated with a random speckle pattern to their top surface. They are then subjected to a tensile load applied along the print path (vertical direction) and a sequence of high-resolution images are taken at increasing strain values. Using a digital image correlation method (33), the experimental strain field is determined (Fig. 3*C*). The same H pattern is also printed using the formulation with lower fiber contents (1.3 vol %) to allow visualization of the heterogeneous fiber orientation using optical (transmission) microscopy (Fig. 3 *D–F*). These images reveal how closely the strain field matches the distribution of fiber orientations. The experimental and numerical results indicate that the strain localizes strongly in the regions where the material has, directionally, a lower stiffness, as characterized in Fig. 2. This is particularly evident in compliant regions confined between regions of higher stiffness, as is the case in the horizontal section of the H. The same phenomenon can also be observed when the same finite-element domain is loaded laterally (Fig. S5). In this case, the strain is largest in the region containing aligned fibers between the serifs of the H (Fig. S5*C*). Perhaps of greater practical importance, the strong control of strain distribution also enables failure initiation in prescribed regions, that is, in this example, failure initiates at the center of the H where the local strain is largest, as denoted by the brightest yellow in the experimental strain field (Fig. 3*C*). Due to the changes in stiffness that occur with different fiber orientations (Fig. 2*A*), a higher local strain would not necessarily become the point of failure. However, tensile experiments show that fiber alignment in our materials has less effect on failure strain (Fig. S7) than it does on stiffness (Fig. 2*A*), and hence programming the stiffness via heterogeneous fiber orientation serves as a means for also manipulating the location of failure. As a result, rotational 3D printing allows one to construct short-fiber reinforced composites that exhibit programmable failure in a controlled manner.

Beyond control of elastic properties and the predominant distribution of strain, the local distribution of fiber alignment also plays an important role in crack propagation during failure (Fig. 4), akin to what is observed in natural composites (8). To determine the effect of fiber alignment on the macroscopic fracture properties, we printed "L"-shaped bars (schematically illustrated in Fig. 4*A*) using a parallel print path, albeit with different rotational patterns. These bars are subsequently mechanically deformed until failure by pulling on each end of the L, as illustrated in Fig. 4*A*. The 90° corner in the geometry produces a stress concentration that assures

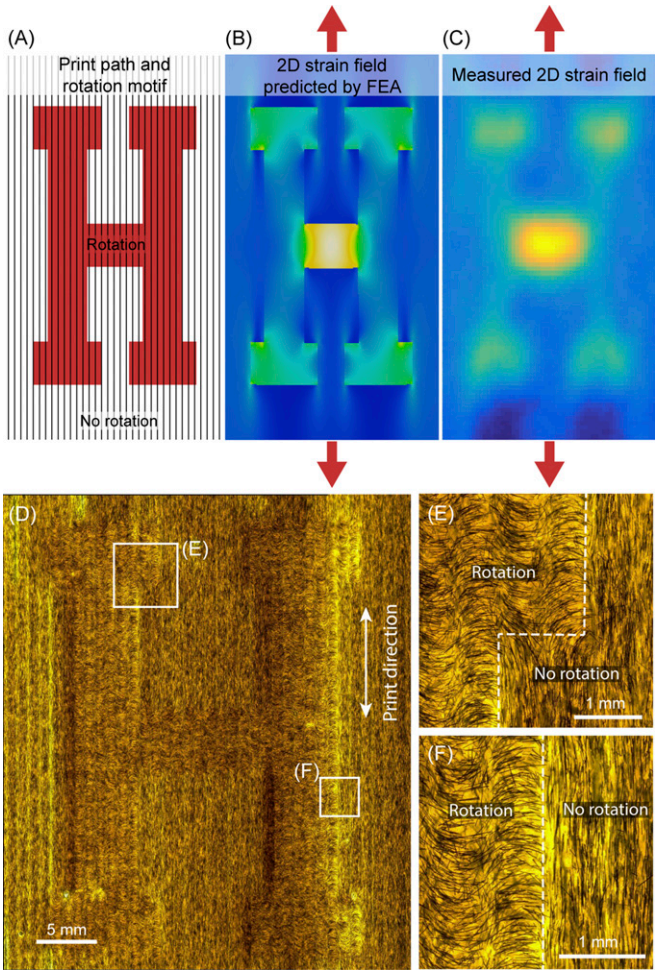

Fig. 3. Programmed fiber alignment, strain, and failure localization. (*A*) Schematic illustration of printed composite that contains an embedded H motif composed of helical fiber arrangements. (*B*) FEA using the elastic properties determined experimentally for each localized region within the printed composites, which predicts a highly complex strain field. (*C*) Experimental strain field measured using digital image correlation (DIC) during tensile testing, which shows the effects of elastic heterogeneity and closely matches that predicted by FEA. (*D*) Optical image of a rotational 3D printed carbon fiber–epoxy composite with an embedded H motif that contains helical fiber arrangements created by locally imposing a controlled rotation speed, while the nozzle is translated along a simple rectilinear raster pattern. (*E* and *F*) Optical images of the denoted regions (white boxes) within a printed composite (1.3 vol % carbon fibers) that reveal abrupt changes in local fiber arrangement within a continuous, uninterrupted print path achieved by rotational 3D printing.

that fracture initiates in this region, regardless of fiber alignment. As controls, we printed L-shaped bars without rotation in this fracture zone, producing a parallel fiber arrangement as well as L-shaped bars with rotation ($R\omega/v = 4.8$) in the fracture region. In both cases, the force is measured during displacement, leading to the responses plotted in Fig. 4*B*. We find that for a fixed print path, localized helical fiber orientation arising from nozzle rotation is associated with more robust mechanical properties (that is, higher applied forces are necessary to initiate failure) and nearly a factor of 2 higher work-to-failure (the area under the force–displacement curve) during fracture propagation (see Table S1 for statistical comparison). This notable improvement in the mechanical response is achieved solely through changes to internal fiber arrangement, without any modifications to external geometry, print path, or material composition. After those tests, we used optical microscopy to examine the fracture patterns for the two types of samples (Fig. 4 *C*–*G*). As expected, fracture initiated in the elbow region of the structure in both cases. However, in samples printed without rotation, the crack proceeds in a straight line parallel to the aligned fibers (Fig. 4 *C* and *D*). By contrast, the propagating crack follows a more complicated pattern in rotationally printed samples that contain a helical fiber arrangement (Fig. 4*E*), in which crack diversion, bridging, and splitting are observed (Fig. 4 *F* and *G*), analogous to fracture patterns observed in natural composites (1, 34–36). Comparing the optical and SEM images of these samples (Fig. 4 *H*–*K*) reveals that the fracture surface of those printed without rotation is much flatter with less fiber pullout and breakage, which is indicative of brittle catastrophic failure (9) and explains their low work-to-failure (Fig. 4*B*). However, individual fibers emerge from, or are broken at, the rougher fracture surface of composites printed with rotation, which lead to their higher work-to-failure. We note that this L-shaped design merely illustrates the potential benefits of imposing helical fiber arrangements for a fixed print path. Ultimately, engineered composites should be constructed through a coordinated optimization of both print path and rotation rate/helical arrangement.

Natural composites, such as shells and bone, are often subjected to mechanical impact and hence their ability to withstand damage is critical to their survival. We investigated the effect of different fiber

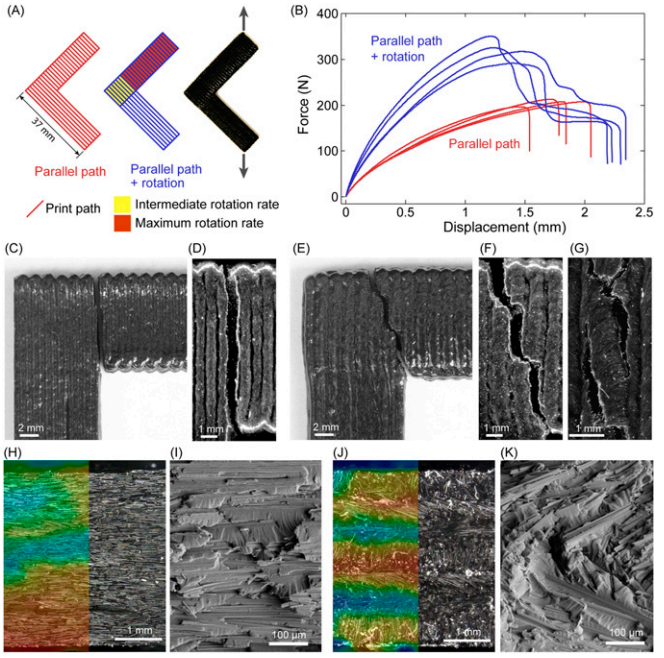

Fig. 4. Fiber arrangement effects on fracture. (*A*) L-shaped composite bars printed with and without rotation were tested in tension by pulling the ends apart. (*B*) Experimental force–displacement data for these samples, which shows that rotation leads to higher stiffness, higher load supported before failure, and higher total energy absorption (work-to-failure) compared with the samples printed without rotation. (*C* and *D*) Optical images of an L-shaped composite bar printed without rotation, showing top-down views after fracture at both low and high magnification, respectively. These samples fractured along the direction of fiber alignment, that is, along the print path. (*E*–*G*) Optical images of an L-shaped composite bar printed with rotation, showing top-down views after fracture at both low and high magnification, respectively. These samples exhibited a more complicated fracture pattern, including crack diversion, bridging, and splitting. (*H* and *I*) Optical image of the fracture surface for a composite printed without rotation; the overlaid color map describes the height field of the fracture surface and corresponding SEM image that shows the fibers are oriented parallel to the surface, respectively. (*J* and *K*) Optical (with overlaid height field) and SEM images, respectively, of the fracture surface for a composite printed with rotation, in which individual fibers emerge from, or are broken at, the rougher fracture surface.

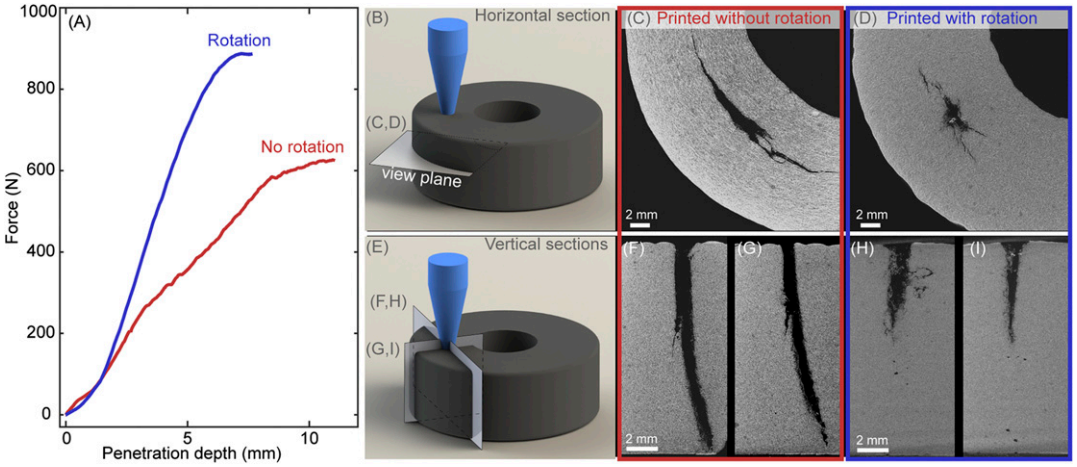

Fig. 5. Composites subjected to puncture loading (in force control). (*A*) To simulate loading conditions frequently encountered by natural composites, specimens are punctured (in load control) with the rotated microstructure withstanding higher forces before failure. (*B*) Schematic view of a printed composite highlighting the horizontal plane viewed by X-ray microtomography. (*C* and *D*) Top surfaces of punctured composites printed without and with rotation, in which the helical arrangement of fibers (akin to those found in osteons in bone) present in the latter sample resulted in a much smaller damaged region than the circumferential fiber arrangements in samples printed without rotation, despite reaching significantly higher applied loads. (*E*) Schematic view of a printed composite highlighting vertical planes viewed by X-ray microtomography. (*F–I*) Cross-sectional views of those vertical planes in punctured composites printed without and with rotation, which reveal that damage penetrates much further below the punch tip in the samples printed without rotation.

orientations on the mechanical properties of our printed composites using puncture tests, similar to techniques used to evaluate the effectiveness of natural armor (37). Cubic samples with high fiber loadings (15.5–18.5 vol %) are printed with an edge length of ~10 mm using the same parallel print path for each layer with ($R\omega/\nu = 3.8$) and without rotation using carbon-fiber-filled, brittle and ductile epoxy resins. After printing and curing, each face of the cubic samples is sanded flat before puncture using a cylindrical punch at a displacement rate of 0.05 mm/s. Representative measurements of the force–displacement response are shown in Fig. S8, with a statistical characterization from additional samples provided in Table S2. Ductile composites with a helical fiber arrangement arising from rotational 3D printing exhibit significantly higher energy absorption (i.e., area under the force–displacement curves) during loading and failure with an increase from 1,868 ± 272 mJ to 3,100 ± 400 mJ, higher failure stress with an increase from 852 ± 80 N to 1,248 ± 150 N, and higher puncture depth at failure with an increase from 3.33 ± 0.29 mm to 4.15 ± 0.15 mm compared with those printed without rotation. For brittle composites with helical fiber arrangements, the observed improvement was even greater, that is, a threefold increase in energy absorption (from 314 ± 82 mJ to 1,067 ± 170 mJ) and a more than twofold higher peak penetration depth (from 0.67 ± 0.13 mm to 1.5 ± 0.09 mm) before failure (a proxy for flaw tolerance). Again, these samples are identical in composition, density, and geometry, varying solely by their internal fiber alignment. Before curing, inks composed of ductile epoxy resin are sufficiently malleable that cubic samples with nominally isotropic fiber arrangements could be molded (rather than printed). Notably, the molded composites performed similarly to printed composites produced with rotation (Table S2).

Another benefit of rotational 3D printing is that the printed architecture can be controlled across multiple length scales. For example, we fabricated composites with high fiber loadings (15.5–18.5 vol %) in the form of osteon-like architectures whose programmed distribution of fiber orientations results in superior damage tolerance (Fig. 5), associated with an ability to withstand higher puncture loads and exhibiting less crack propagation away from the site of loading. Osteons are microstructural features in bone with a characteristic cylindrical geometry and a canal feature in the core. Within their cylindrical walls, fibers are arranged radially with respect to the cylinder. In the absence of rotation, the printed composite cylinders contain a circumferential fiber alignment (the direction of the print path) rather than the desired radial distribution. By contrast, composite cylinders produced by rotational 3D printing ($R\omega/\nu = 3.8$) possess helical fiber arrangements that are oriented radially in an osteon-like manner. Natural materials often encounter concentrated puncture loading (37) (for example, due to a predator), which can best be categorized as loading in force control rather than displacement control. To assess their ability to withstand puncture stresses without failing, we loaded the printed osteon-like structures using a similar puncture approach described above (see also Fig. S8), but using force control (Fig. 5*A*). Those with helical fiber alignment are able to withstand much higher puncture forces before catastrophic failure (Fig. 5*A*) compared with those with circumferentially aligned fibers. After these tests, we examined the internal damage of the specimens using μCT along different planes (Fig. 5 *B–I*). Despite supporting higher loads during puncture, the rotationally printed samples exhibited less penetration of the punch, and, thus, less internal damage (associated with both lateral crack growth perpendicular to the punch, Fig. 5 *B–D*, and vertical crack growth parallel with the punch, Fig. 5 *E–I*). Higher forces are required to achieve inelastic penetration to any depth for rotationally printed samples compared with those produced without rotation.

In summary, we have demonstrated an additive manufacturing method for creating engineered composites with controlled fiber orientation, microstructural complexity, and mechanical performance akin to natural systems. Specifically, we have used rotational 3D printing to construct carbon fiber–epoxy composites with prescribed fiber arrangements that result in superior combinations of stiffness, toughness, and damage tolerance. Our approach also enables programmed strain and failure distribution by patterning adjacent regions with distinct mechanical properties (e.g., anisotropic vs. isotropic). Engineered composites with helical fiber arrangements have been produced that exhibit enhanced damage tolerance akin to natural systems. Due to its simplicity and ease of implementation, rotational 3D printing can be readily extended to other anisotropic filler and matrix combinations, where control over filler orientation would enable programmed electrical, optical, or thermal properties.

Methods

Composite Inks. Multiple composite inks are produced using two different epoxy resins. One of these resins (Momentive Epon 826), denoted as the brittle epoxy resin, yields matrices with higher stiffness and a more brittle response. The other resin (Momentive Epon 8131), denoted as the flexible epoxy resin, yields matrices with lower stiffness and a higher strain of failure. The inks based on Epon 826 are closely related to those developed in our earlier work (18), but they contain a higher carbon fiber loading. To produce this ink, 6 g of dimethyl methylphosphonate, 9.5 g of nanoclay (Nanocor I.34TCN), and 21.5 g of milled carbon fibers (Dialead K223HM; Mitsubishi Plastics) were added to 60 g of epoxy resin (Momentive Epon 826). These components are mixed under vacuum for ~7 min (Flacktek SpeedMixer). Subsequently, 3 g of a curing agent (Basionics VS03) is added, followed by an additional mixing cycle (~4 min). An alternative ink formulation with lower carbon fiber loading (1.3 vol %) is used to characterize fiber orientation with optical microscopy. The flexible inks are produced using 9.9 g fumed silica (CAB-O-SIL TS-530; Cabot) rather than the nanoclay, 24.0 g of milled carbon fibers, and 60 g resin. As before, these components are mixed, 4.3 g of VS03 is added, followed by a second mixing step. All inks are loaded into 3-mL syringes (Nordson EFD) and centrifuged to remove any trapped air.

Rotational 3D Printing. A rotating Luer lock coupling is joined to the end of the syringe, and nozzles of various sizes (410-840 μm) are then connected. The rotating coupling element enables the nozzles to rotate freely relative to the syringe barrel. A grooved belt is used to couple the rotation of the nozzle tip to a stepper motor, which directly interfaces with the 3D motion control system used to translate the printhead (Aerotech). We note that misalignment of the nozzle with respect to the axis of rotation can introduce defects into the printed parts. All print paths are created by writing the appropriate G-code commands. Rotation is applied in a programmed manner, coordinated directly with motion in x, y, and z. Each ink is extruded from the syringe through the nozzle using volumetric control, applied via a positive displacement pump (Nordson Ultimus IV), onto polytetrafluoroethylene-coated aluminum foil on top of a glass substrate. After printing, the composites are placed in an oven at elevated temperature to cross-link the epoxy resin. Composites based on the brittle epoxy resin (Epon 826) are cured in the oven for 15 h at 100 °C, followed by a high-temperature step for 2 h at 220 °C, following the procedure in ref. 18, while those based on flexible epoxy resin (Epon 8131) are cured in the oven for 35 h at 100 °C.

Mechanical Characterization. Mechanical tests are carried out using a commercial quasistatic test system (Instron 5566) to control displacement and measure the load across the specimen. To obtain an accurate measure of material stiffness, the strain of the sample during loading is measured via high-resolution video and subsequent custom correlation scripts in MATLAB. These tests are conducted at a strain rate of 10^{-3}·s^{-1}. To measure strain fields, samples are spray painted to produce a random pattern of white dots. Displacement is incremented discretely using the quasistatic test system while high-resolution photographs are acquired and subsequently analyzed using digital image correlation routines in MATLAB (33). Puncture tests are carried out using the same quasistatic test system at a displacement rate of 0.05 mm/s equipped with a custom steel, cylindrical punch (1.3-mm tip diameter).

Structural Characterization. The fiber alignment and fracture characteristics of the printed and cured carbon fiber–epoxy composites are measured optically (Keyence VHX), by SEM, and X-ray μCT (HMXST225; Nikon Metrology X-Tek).

Finite-Element Analysis. Finite-element analysis (FEA) is carried out using Abaqus/Standard 6.14 (Dassault Systems) with a plane stress assumption and linear elastic constitutive behavior. In this analysis, the elastic properties are chosen to represent the carbon fiber–epoxy composites printed with and without rotation to define the H and surrounding material, respectively. The H region is assumed to be isotropic with Young's modulus $E = 2.5$ GPa, and Poisson's ratio $\nu = 0.34$. The surrounding region (with highly directional fiber orientation) is assumed to be anisotropic with the following engineering elastic constants: $E_1 = 10.4$ GPa, $E_2 = 1.7$ GPa, $E_3 = 1.7$ GPa, $\nu_{12} = 0.36$, $\nu_{13} = 0.52$, $\nu_{23} = 0.3$, $G_{12} = 1.04$ GPa, $G_{13} = 1.04$ GPa, and $G_{23} = 0.56$ GPa, where the 1 direction is oriented parallel to the print direction within the samples. Simulations are conducted by fixing the lower edge of the domain in the vertical direction and applying a vertical displacement to the upper edge of the domain to result in a global average tensile strain of 1.667%.

ACKNOWLEDGMENTS. The authors gratefully acknowledge Mr. Teng-Sing Wei and Mr. Hao-Yu Greg Lin for their help with X-ray μCT, Dr. James Weaver for performing SEM related to this study, and Ms. Katharina Kroll and Prof. John L. Bassani for helpful suggestions. This work is supported by the Vannevar Bush Faculty Fellowship Program sponsored by the Basic Research Office of the Assistant Secretary of Defense for Research and Engineering and funded by Office of Naval Research Grant N00014-16-1-2823. J.A.L. thanks the GETTYLAB for their generous donation in support of our research.

1. Launey ME, Buehler MJ, Ritchie RO (2010) On the mechanistic origins of toughness in bone. *Annu Rev Mater Res* 40:25–53.
2. Da Silva A, Kyriakides S (2007) Compressive response and failure of balsa wood. *Int J Solids Struct* 44:8685–8717.
3. Marklund E, Varna J (2009) Modeling the effect of helical fiber structure on wood composite elastic properties. *Appl Compos Mater* 16:245–262.
4. Qing H, Mishnaevsky L, Jr (2009) 3D hierarchical computational model of wood as a cellular material with fibril reinforced, heterogeneous multiple layers. *Mech Mater* 41:1034–1049.
5. Reiterer A, Lichtenegger H, Tschegg S, Fratzl P (1999) Experimental evidence for a mechanical function of the cellulose microbril angle in wood cell walls. *Philos Mag A* 79:2173–2184.
6. Barnett JR, Bonham VA (2004) Cellulose microfibril angle in the cell wall of wood fibres. *Biol Rev Camb Philos Soc* 79:461–472.
7. Donaldson L (2008) Microbril angle: Measurement, variation and relationships–A review. *IAWA J* 29:345–386.
8. Weaver JC, et al. (2012) The stomatopod dactyl club: A formidable damage-tolerant biological hammer. *Science* 336:1275–1280.
9. Hull D, Clyne T (1996) *An Introduction to Composite Materials* (Cambridge Univ Press, Cambridge, UK), pp 9–29.
10. Zhang K, Wang Y (1998) Biomimetic study on helical fiber composites. *J Mater Sci Technol* 14:29–32.
11. Apichattrabrut T, Ravi-Chandar K (2006) Helicoidal composites. *Mech Adv Mater Struct* 13:61–76.
12. Marshall DB, Cox BN (2008) Integral textile ceramic structures. *Annu Rev Mater Res* 38:425–443.
13. Zhang Y, et al. (2015) Fabrication and mechanical characterization of 3D woven Cu lattice materials. *Mater Des* 85:743–751.
14. Kazemahvazi S, Khokar N, Hallstrom S, Wadley H, Deshpande V (2016) Confluent 3D-assembly of fibrous structures. *Compos Sci Technol* 127:95–105.
15. Raney JR, Lewis JA (2015) Printing mesoscale architectures. *MRS Bull* 40:943–950.
16. Calvert P, Lin TL, Martin H (1997) Extrusion freeform fabrication of chopped-fibre reinforced composites. *High Perform Polym* 9:449–456.
17. Shofner M, Lozano K, Rodriguez-Macias F, Barrera E (2003) Nanofiber-reinforced polymers prepared by fused deposition modeling. *J Appl Polym Sci* 89:3081–3090.
18. Compton BG, Lewis JA (2014) 3D-printing of lightweight cellular composites. *Adv Mater* 26:5930–5935.
19. Tekinalp HL, et al. (2014) Highly oriented carbon fiber-polymer composites via additive manufacturing. *Compos Sci Technol* 105:144–150.
20. Gladman AS, Matsumoto EA, Nuzzo RG, Mahadevan L, Lewis JA (2016) Biomimetic 4D printing. *Nat Mater* 15:413–418.
21. Malek S, Raney JR, Lewis JA, Gibson LJ (2017) Lightweight 3D cellular composites inspired by balsa. *Bioinspir Biomim* 12:026014.
22. Lewis JA (2006) Direct ink writing of 3D functional materials. *Adv Funct Mater* 16:2193–2204.
23. Smay JE, Cesarano J, III, Lewis JA (2002) Colloidal inks for directed assembly of 3D periodic structures. *Langmuir* 18:5429–5437.
24. Gratson GM, Xu M, Lewis JA (2004) Microperiodic structures: Direct writing of three-dimensional webs. *Nature* 428:386.
25. Ahn BY, et al. (2009) Omnidirectional printing of flexible, stretchable, and spanning silver microelectrodes. *Science* 323:1590–1593.
26. Bell JP (1969) Flow orientation of short fiber composites. *J Compos Mater* 3:244–253.
27. Farkash M, Brandon D (1994) Whisker alignment by slip extrusion. *Mater Sci Eng A* 177:269–275.
28. Collino RR, et al. (2015) Acoustic field controlled patterning and assembly of anisotropic particles. *Extreme Mech Lett* 5:37–46.
29. Collino RR, et al. (2016) Deposition of ordered two-phase materials using microfluidic print nozzles with acoustic focusing. *Extreme Mech Lett* 8:96–106.
30. Martin JJ, Fiore BE, Erb RM (2015) Designing bioinspired composite reinforcement architectures via 3D magnetic printing. *Nat Commun* 6:8641.
31. Kokkinis D, Schaffner M, Studart AR (2015) Multimaterial magnetically assisted 3D printing of composite materials. *Nat Commun* 6:8643.
32. Compton BG, et al. (2018) Direct-write 3D printing of NdFeB bonded magnets. *Mater Manuf Processess* 33:109–113.
33. Eberl C, Gianola DS, Hemker KJ (2010) Mechanical characterization of coatings using microbeam bending and digital image correlation techniques. *Exp Mech* 50:85–97.
34. Kamat S, Su X, Ballarini R, Heuer AH (2000) Structural basis for the fracture toughness of the shell of the conch Strombus gigas. *Nature* 405:1036–1040.
35. Nalla RK, Kinney JH, Ritchie RO (2003) Mechanistic fracture criteria for the failure of human cortical bone. *Nat Mater* 2:164–168.
36. Launey ME, Chen P-Y, McKittrick J, Ritchie RO (2010) Mechanistic aspects of the fracture toughness of elk antler bone. *Acta Biomater* 6:1505–1514.
37. Zhu D, Szewciw L, Vernerey F, Barthelat F (2013) Puncture resistance of the scaled skin from striped bass: Collective mechanisms and inspiration for new flexible armor designs. *J Mech Behav Biomed Mater* 24:30–40.

Supporting Information

Raney et al. 10.1073/pnas.1715157115

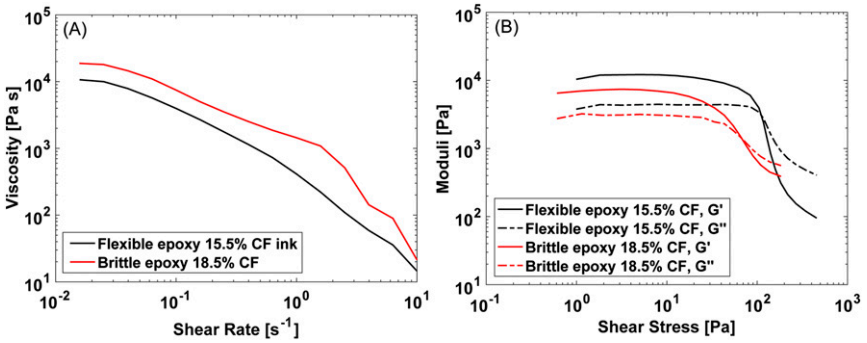

Fig. S1. (*A*) Log–log plot of ink viscosity as a function of shear rate and (*B*) shear storage (G') and loss (G'') moduli as a function of shear stress for the carbon-fiber-filled epoxy resin inks.

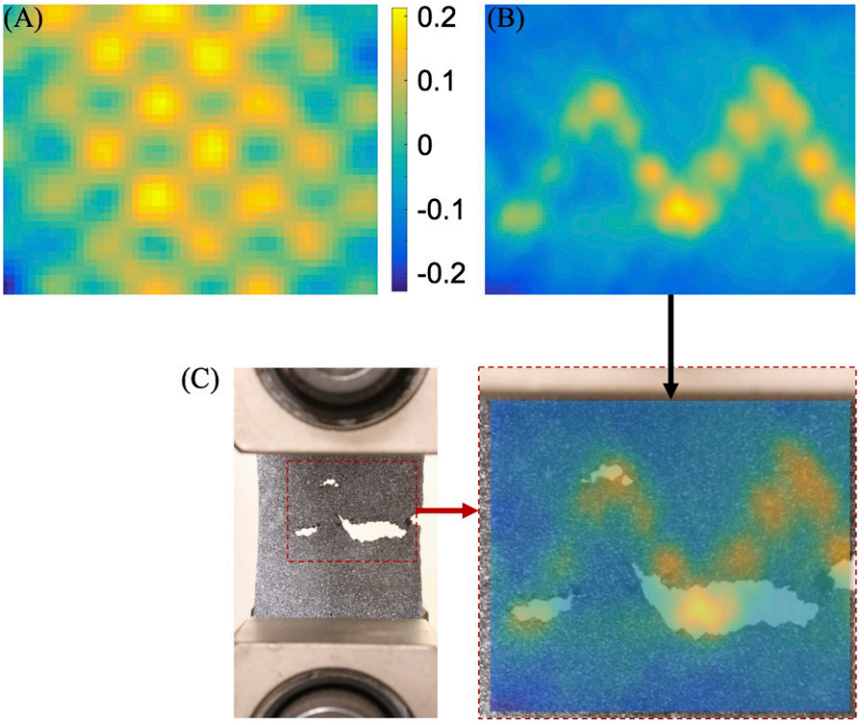

Fig. S2. Experimental strain measurements obtained on samples rotationally printed with fiber orientations that varied in (*A*) checkerboard and (*B*) sinusoidal patterns (18.6-mm × 24-mm areas shown). The reported values correspond to the observed strain normalized by the mean strain. These data were acquired from a sequence of photographs taken at increasing values of imposed displacement, followed by image analysis using DIC. (*C*) Photograph of the sample with the sinusoidal pattern taken immediately after failure (*Left*) and subsequently overlaid on the strain field obtained immediately before failure (from *B*).

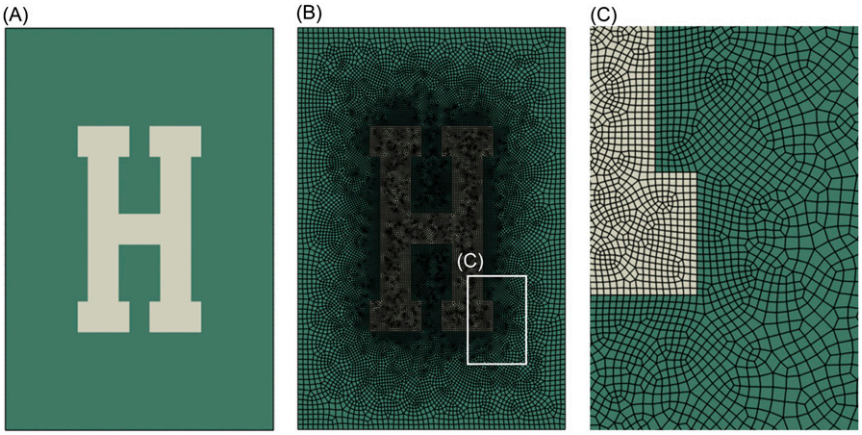

Fig. S3. (*A*) FEA carried out on 40-mm × 60-mm geometric domain, in which the beige and green regions are defined to have elastic properties representative of the carbon fiber–epoxy composite printed with and without rotation, respectively. (*B*) A graded mesh scheme is used to more fully resolve the elastic strain fields at the sharp transitions between the isotropic H domain and the anisotropic surrounding material. (*C*) Detailed view of the graded mesh.

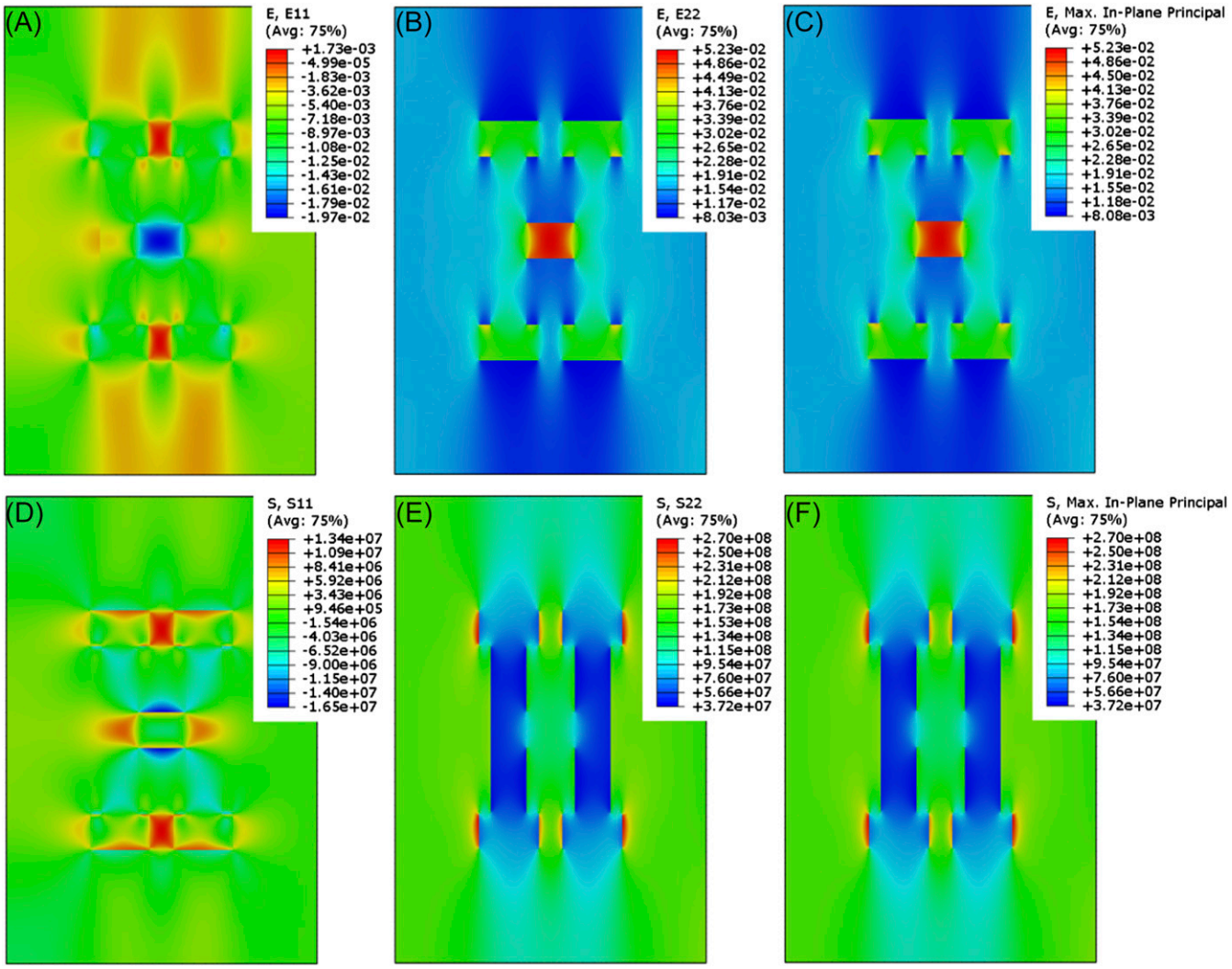

Fig. S4. Strain and stress fields for the finite-element domain subject to 1.667% strain in the vertical direction. (*A*) Elastic strain in the horizontal direction. (*B*) Elastic strain in the vertical direction. (*C*) Maximum in-plane principal elastic strain. (*D*) Direct stress in the horizontal direction. (*E*) Direct stress in the vertical direction. (*F*) Maximum in-plane principal stress.

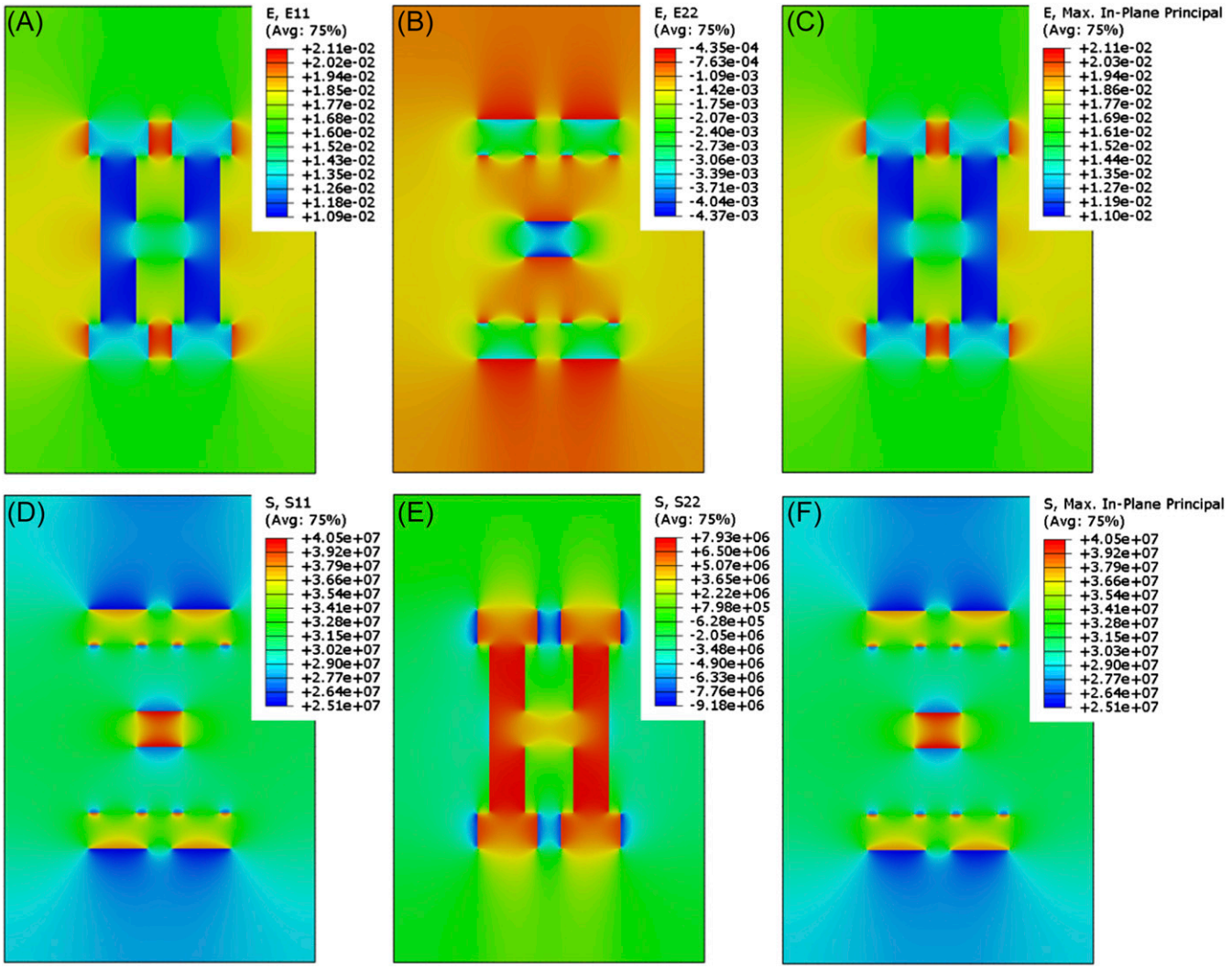

Fig. S5. Strain and stress fields for the finite-element domain subject to 1.667% strain in the horizontal direction. (*A*) Elastic strain in the horizontal direction. (*B*) Elastic strain in the vertical direction. (*C*) Maximum in-plane principal elastic strain. (*D*) Direct stress in the horizontal direction. (*E*) Direct stress in the vertical direction. (*F*) Maximum in-plane principal stress.

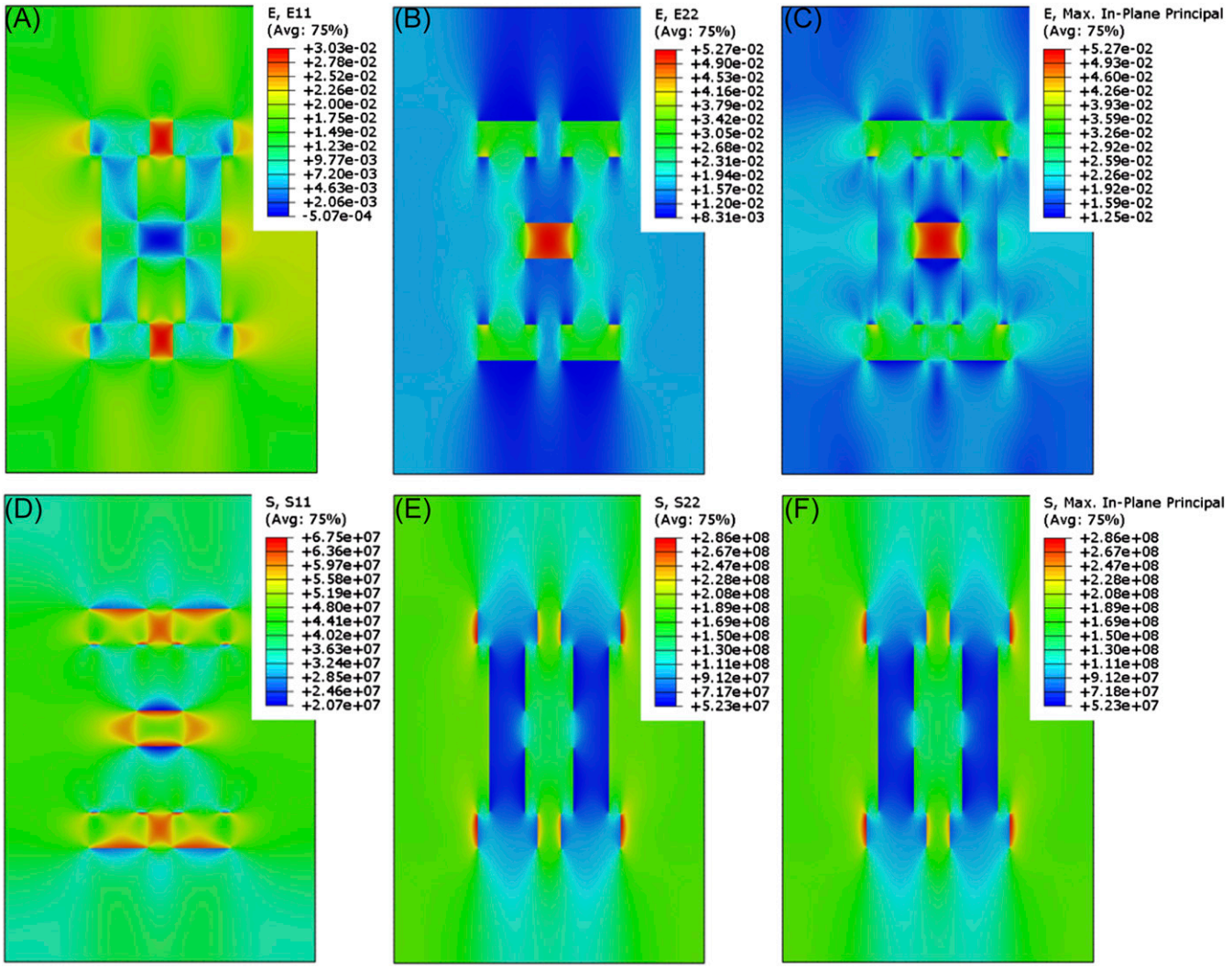

Fig. S6. Strain and stress fields for the finite-element domain subject to equibiaxial strain of 1.667%. (*A*) Elastic strain in the horizontal direction. (*B*) Elastic strain in the vertical direction. (*C*) Maximum in-plane principal elastic strain. (*D*) Direct stress in the horizontal direction. (*E*) Direct stress in the vertical direction. (*F*) Maximum in-plane principal stress.

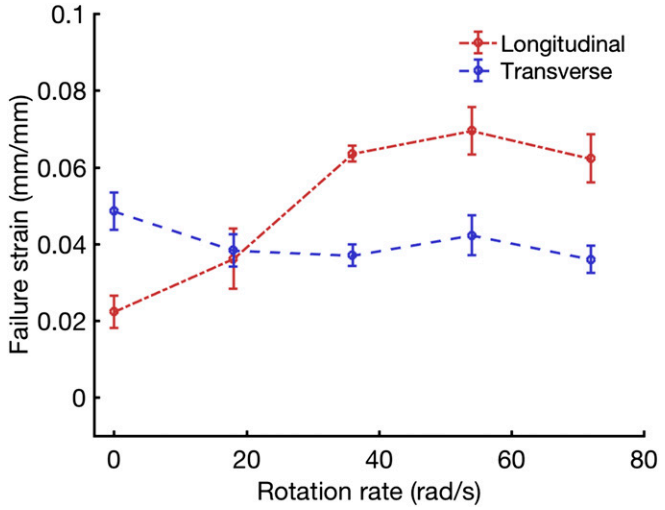

Fig. S7. Failure strain measured experimentally for the samples tested in Fig. 2.

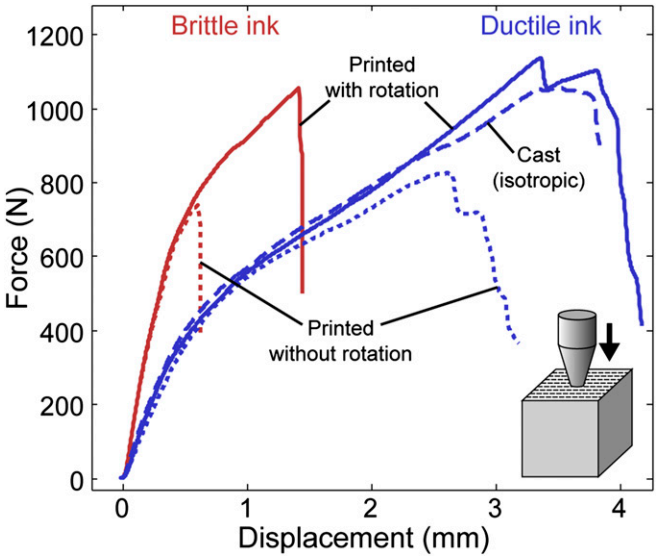

Fig. S8. Load–displacement curves for composite cubes composed of short carbon fibers in a brittle or ductile epoxy matrix printed with or without rotation and subjected to quasistatic, instrumented puncture (displacement control).

Table S1. Summary of mechanical properties for tests reported in Fig. 4*B*

Mechanical property	No rotation	Rotation
Energy absorption, mJ	249 ± 35	490 ± 35
Peak force, N	226 ± 44	321 ± 24
Initial stiffness, N/mm	432 ± 12	812 ± 106
Maximum displacement, mm	1.81 ± 0.21	2.27 ± 0.07

Table S2. Mechanical behavior of printed composite cubes subjected to indentation

Sample type	Energy absorption, mJ	Peak force, N	Maximum displacement, mm
Brittle epoxy			
No rotation	314 ± 82	745 ± 41	0.67 ± 0.13
Rotation	1,067 ± 170	1,066 ± 49	1.5 ± 0.09
Flexible epoxy			
No rotation	1,868 ± 272	852 ± 80	3.33 ± 0.29
Rotation	3,100 ± 400	1,248 ± 150	4.15 ± 0.15
Cast	3,460 ± 1,000	1,216 ± 280	4.35 ± 0.60

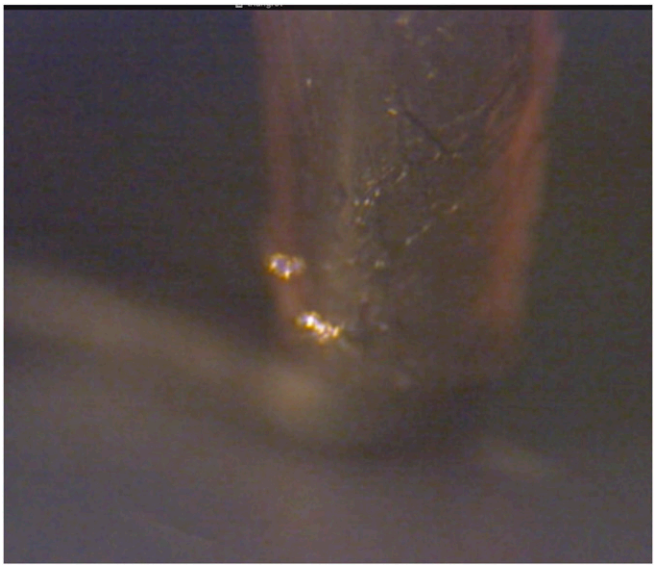

Movie S1. Close-up video of rotational 3D printing of carbon fiber–epoxy composites. The rotation events are synchronized with translation to allow fiber orientation to be precisely and locally controlled throughout the fabricated object.

Movie S1